ELSEVIER

International Journal of Mass Spectrometry 177 (1998) 63–81

International Journal of Mass Spectrometry

External source Fourier transform ion cyclotron resonance mass spectrometry by using a split-pair magnet

W.D. Reents, Jr.*, M.L. Mandich, A.M. DeSantolo

Lucent Technologies, Bell Laboratories, Murray Hill, New Jersey 07974, USA

Received 27 August 1997; accepted 12 January 1998

Abstract

A new instrument has been designed, built, and tested for high performance Fourier transform ion cyclotron resonance mass spectrometry (FTICRMS) that allows operation at gas pressures of up to ~20 Torr in the ion source and up to ~0.01 Torr in the ion trap. FTICRMS performance is not compromised at these pressures due to an external, high throughput ion source and pulsed gas introduction/rapid gas evacuation of the vacuum chamber at the trapped ion cell. This system is the first to retain ions at 0.01-Torr gas pressure in the ion trap with high sensitivity. This performance is achieved while obtaining high mass resolution and ppm mass accuracies. (Int J Mass Spectrom 177 (1998) 63–81) © 1998 Elsevier Science B.V.

Keywords: Clusters; Fourier transform ion cyclotron resonance mass spectrometry; Split-pair magnet; External ion source

1. Introduction

Fourier transform ion cyclotron resonance mass spectrometry (FTICRMS) is a high performance mass spectrometry technique that offers ultrahigh mass resolution, sub-ppm mass accuracy, and the ability to hold onto and manipulate ions for millisecond to hour time periods [1]. We have developed an FTICRMS by utilizing a differentially pumped pulsed ion source coupled to a custom-built split-pair superconducting magnet that demonstrates high sensitivity while maintaining high mass resolution, and accurate ion abundances.

The external, differentially pumped ion source is a critical component of our new FTICRMS instrument. As has been shown by other workers, such sources allow for ion formation at the high pressures required to make some ion species while maintaining the optimum low pressure detection required for ultrahigh mass resolution. Operating at pressures of 5–30 Torr, our ion source produces intense pulsed ion beams while the FTICRMS trapped ion cell is maintained at a base pressure of 1×10^{-9} Torr. These source pressures are sufficiently great that large clusters and particles can be formed in situ from ablated materials. These pressures also serve to cool and narrow the kinetic energy distribution of the ions produced from the source.

Ultrahigh mass resolution and high sensitivity are achieved by using the large bore/split-pair design of our magnet. This magnet design enables us to use collisional relaxation to collapse the size of the ion population soon after it arrives at the trapped ion cell. The nominal pressure in the ion cell is elevated by launching a high pressure (0.01 Torr) pulse of

* Corresponding author.

PII S1387-3806(98)14010-1

quenching gas perpendicular to the axis of the magnetic field via ports in the split between the magnet pairs. The gas pulse greatly increases the detected ion signal by collisionally relaxing the ions to the center of the trapped ion cell. This technique somewhat resembles the quadrupolar excitation method with the exception that no rf excitation is required; the high pressure collisions are sufficient to collapse the ion cloud to the center of the cell [2]. Similarly, we can also chemically probe the trapped ions with pulses of reactive gases. The high conductance of the large bore along the axis of the magnetic field then allows for this gas pulse to be quickly pumped away before initiating ion detection. For example, a nominal gas pressure of 0.01 Torr in the ion cell can be reduced to $<1 \times 10^{-8}$ Torr in $\sim$2 s. Thus, we attain high ion sensitivity and retain high mass resolution. Our design represents an improvement over other systems where collisional relaxation is employed. In order to reduce the gas pressure during detection, these other instruments use either a pulsed gas source [3] or a cryopumped cell [1a]. However, because these systems lack sufficient conductance, the former solution results in a working gas pressure during detection with a higher than desirable vacuum system pressure whereas the latter limits the ability to chemically probe the trapped ions.

Our magnet also has a large homogeneous region that accommodates a large ion cell volume. This feature is exploited to trap very large ion populations that enable us to survey wide mass ranges and obtain accurate isotopic abundances with a single mass scan. Such large ion populations can be trapped without compromising high mass resolution and relative ion abundances [4] both of which are degraded by space-charge interactions. This represents an important improvement over conventional cell sizes where high mass resolution can only be attained at extremely low ion loadings, limiting both sensitivity, and, in the case of biomolecules, accurate isotopic abundance ratios from a single mass spectrum.

This article describes the design and performance of this instrument. We demonstrate its capabilities for large mass range and particle generation with elemental clusters of carbon, silicon, vanadium, and cobalt.

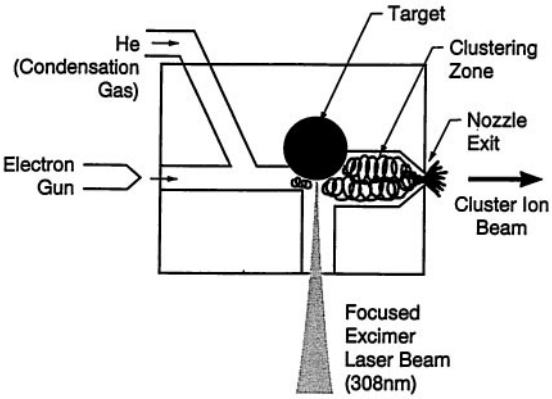

Fig. 1. Source for producing clusters and particles by laser ablation of a target into a condensation gas flow. The material removed by the laser is entrained in the clustering zone where particle growth occurs. Substantial numbers of ions result from the plasma created by the ablation laser. Additional ionization can be achieved with the approximately 1 kV electrons emitted from an electron gun into a 0.005-in.-diameter orifice located at the back of the source. The flowing condensation gas sweeps both neutral and charged particles out of the source through a conical nozzle where they undergo a supersonic expansion. Charged clusters are extracted from the expanding neutral beam and accelerated into an electrostatic ion guide.

2. Experimental

2.1. Ion source

Synthesis of clusters and nanoparticles is accomplished by condensation of the appropriate elemental materials in a cooling gas. The source follows the designs of previously described “continuous gas flow” cluster sources [5] and is shown schematically in Fig. 1. A stainless steel chamber houses a solid 1/4-in.-diameter target rod of the raw elemental material(s) of interest. Target rods used in this study are carbon (99.999% purity), silicon (99.9999% purity), vanadium (99.7% purity), and cobalt (99.95% purity). The rod is positioned at the side of a channel through which 5–20 Torr of helium carrier gas is flowed continuously at a rate of 100–500 sccm. The entire

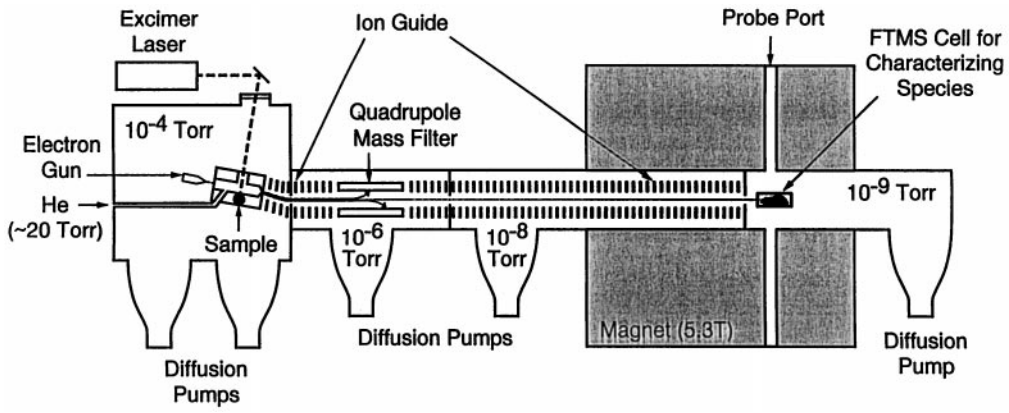

Fig. 2. Overall schematic of the instrument. The off-axis source and source ion optics are located in the first stage of differential pumping (10^{-4} Torr). Ions are extracted from the source and accelerated into an electrostatic ion guide that moves them from the source region and loads them into the FTICRMS trapped ion cell located in the room temperature bore of a 5.3 Tesla superconducting solenoid magnet. This ion guide incorporates focusing through three conductance limiting orifices that separate intermediate stages of differential pumping (at 10^{-6} and 10^{-8} Torr) between the source and the FTICRMS trapped ion cell at 10^{-9} Torr. The ion mass distribution can be narrowed prior to arrival at the trapped ion cell by using the quadrupole mass filter. Just before the trapped ion cell, the ions are decelerated and focused for optimal transmission through a conductance-limiting orifice located in front of the cell. Cooling and reagent gases as well as spectroscopic probes can be introduced through the four probe ports that access the trapped ion cell perpendicular to the bore.

source can be cooled to ~−140 °C if desired by flowing liquid nitrogen through a cooling block mounted on the side of the source chamber. Cluster synthesis is initiated by pulsed laser evaporation of material from the target rod. Suitable amounts of material are ablated by using ~160-mJ output of an XeCl excimer laser (308 nm, 40 ns pulse width) focused with a 400-mm focal length lens onto the rod. At our wavelength and pulse energies, laser ablation creates a plasma above the surface of the rod that contains ionic and neutral species from the target plus electrons and ionized carrier gas species. This plasma forms as a plume above the rod and serves to inject the laser ablated species into the cooling gas flow. It is crucial to continuously rotate and translate the target during the ablation process to avoid creating a deep hole in the target rod. Such holes cause erratic source performance, undoubtedly because they disrupt the formation and extent of the plasmas that lead to cluster growth. Large particles grow in the carrier gas within the confines of the channel between the target rod and the nozzle exit from the source. The helium carrier gas can also be doped with molecular species to introduce additional reagents to the growing particles.

Particles form by bimolecular association of neutral atoms and molecules with both charged and neutral atoms and molecules. The presence of the helium carrier gas is crucial because it provides collisions that stabilize the various associated species throughout the growth process. In the present source configuration, the growing particles spend up to 700 μs in the source which allows for tens of thousands of cooling collisions with the helium carrier gas. The presence of the carrier gas at moderate pressures and flows also slows the migration and loss of neutral and ionized species to the walls. The initial plasma created by the laser contains a large fraction of ionized particles; further ionization can be accomplished if desired with the output of an electron gun positioned behind the source (Fig. 1). Ions persist under the conditions of the source, which provides an intense beam of both positively and negatively charged species as well as neutrals. Note that the pulsed laser evaporates a pulse of material into a continuous gas flow. Thus, although a continuous stream of carrier

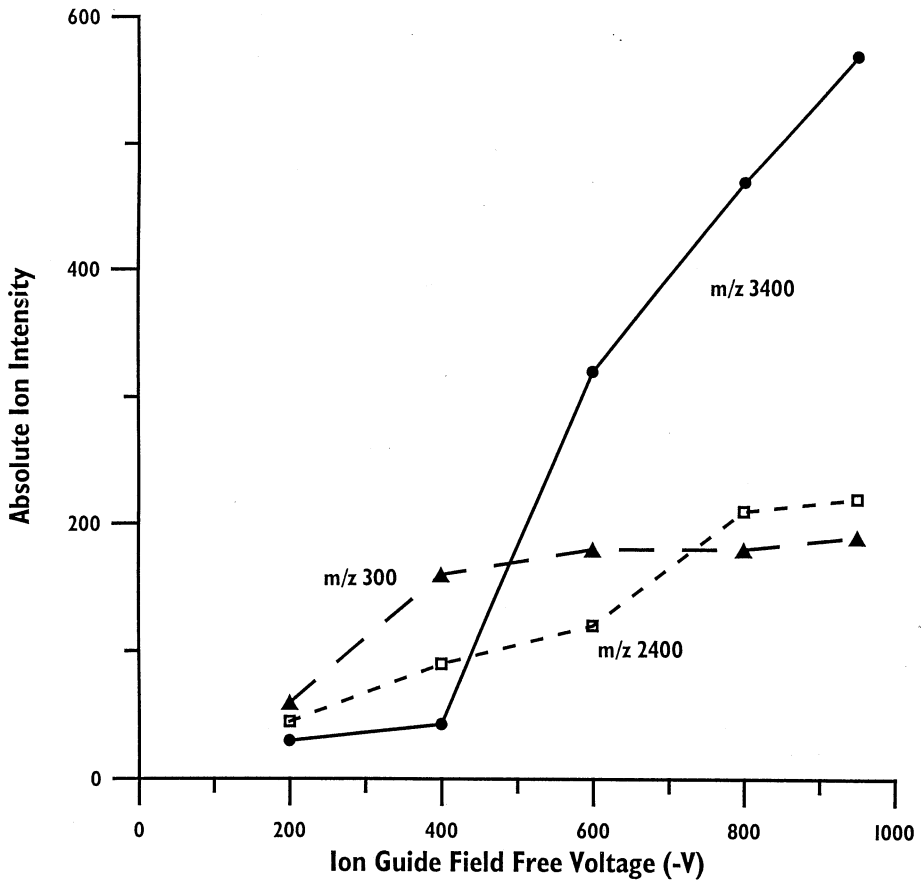

Fig. 3. Illustration of ion guide transmission efficiency as a function of both field free voltage and ion mass. A significant mass dependence for the transmission is observed. By −800 V, transmission efficiency is constant for ions up to m/z 2400. At m/z 3400 and presumably higher masses, transmission has not leveled off. Higher voltages are still required. The bulk of the ions detected under these conditions have masses around 3400 U or larger. Ion intensities are shown in arbitrary units. Note that the isotopic distribution at higher masses causes a decreased intensity for any one mass. Thus, the relative intensity of the larger clusters compared to C_{25}^+ (m/z 300) are greater than indicated by the single mass relative intensities shown in the graph.

gas exits the source, the clusters and particles are formed in discontinuous bursts. Diffusion of the various species in the carrier gas spreads this burst over 300–1000 μs, which is considerably longer than the initial ∼100-ns pulse of material ablated from the rod. At typical ablation laser repetition rates of 50 Hz, however, individual bursts remain separated.

Particles and carrier gas exit the source via a conical nozzle into a medium vacuum of $\sim 10^{-4}$ Torr. Several events occur at this nozzle exit. First, within the throat of the nozzle, the carrier gas and particles undergo a supersonic expansion. With the source operating at room temperature and the current nozzle orifice diameter of 1 mm, this expansion is sufficient to translationally cool the helium to ∼30 K. Additional cooling to ∼5 K can be achieved by cooling the source to −140 °C. Particles contained within the helium carrier gas undoubtedly do not achieve full expansion and therefore have a somewhat higher thermal velocity distribution. Second, particle growth stops as the gas density abruptly falls, and the distribution of particles becomes “frozen.” Third, charged particles are accelerated by the field of the first element of an electrostatic ion guide. This extracts

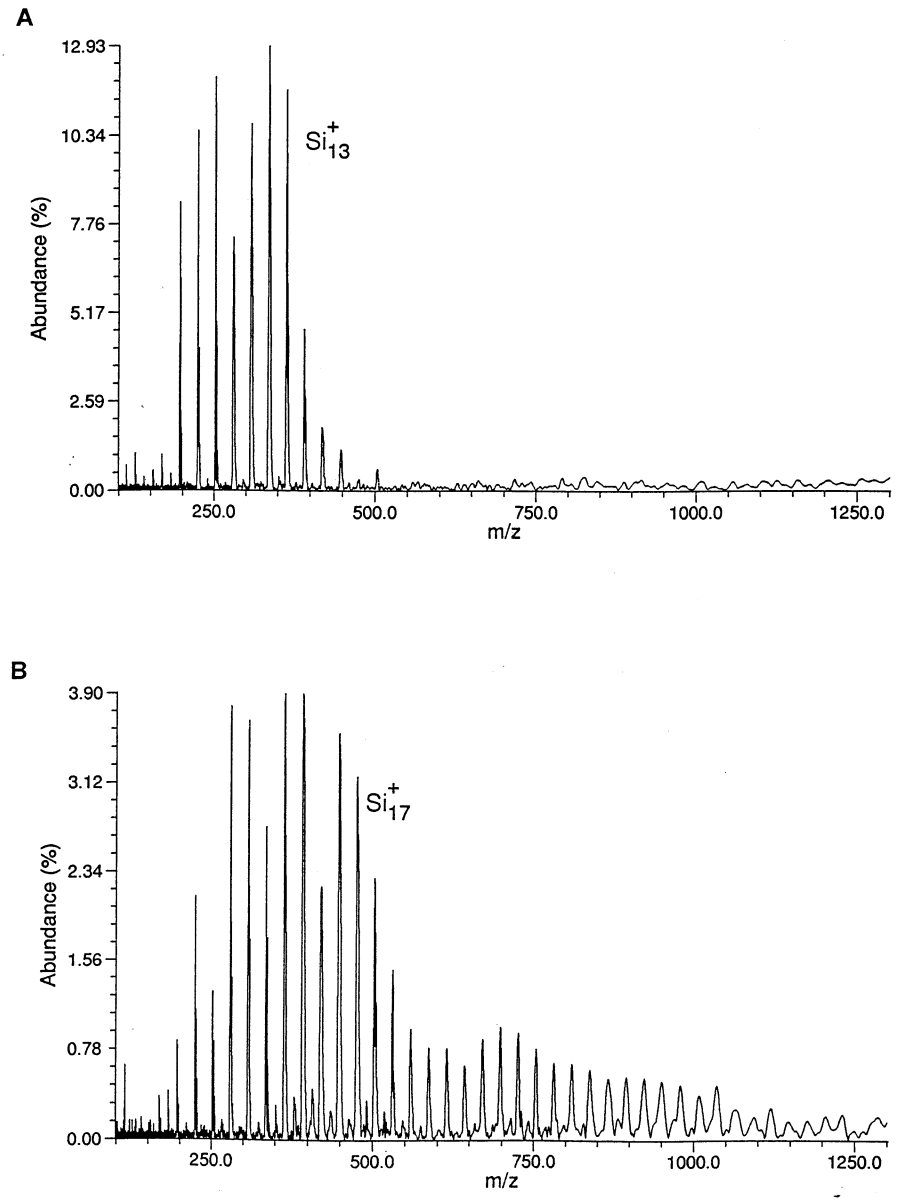

Fig. 4. Comparison of silicon cluster positive ion distribution obtained from (A) a fresh silicon rod and from (B) the same rod after being subjected to several hours of laser ablation. The increase in ion cluster size from the "aged" rod may derive from a channel being formed in the rod as explained in the text.

them from the neutrals and loads them into the ion guide described below, which transports them to the trapped ion cell of a Fourier transform ion cyclotron resonance mass spectrometer. Typical ion currents exiting the source are 100–400 pC/pulse. This translates into peak currents of $>$ 100 nA.

2.2. Electrostatic ion guide

The high pressure operation of the source requires multiple stages of differential pumping to achieve the high vacuum required in the mass spectrometer. At the same time, high particle densities are desired in

the trapped ion cell, requiring efficient transfer of ions from the source through the series of conductance-limiting orifices (6 mm) separating the various pumping stages (Fig. 2). Previous workers have reported ion guide designs that successfully interface a high pressure ion source region to an FTICRMS trapped ion cell [6]. We designed our own ion guide to transport the short, intense ion currents expected from our laser ablation source as well as to accommodate our off-axis ion source.

Our ion guide design is based on optimized ion trajectories and incorporates ion extraction, einzel lenses, *X*/*Y* deflection, and an exponential deceleration field to maximize ion throughput from the source to the trapped ion cell [7]. The physical design uses only materials that are compatible with high magnetic fields. Four stages of differential pumping separated by three 6-mm-diameter orifices incorporate high speed pumps to reduce the pressure from 20 Torr in the source to 10^{-4} Torr in the source chamber and ultimately to 10^{-9} Torr in the mass spectrometer (Fig. 2). The ion guide conductance orifices have been optically aligned so as to allow optimum ion travel along the true magnet axis, thereby enhancing ion transmission (see below). The ion guide can incorporate a quadrupole mass filter section for selecting out a portion of the mass distribution before the ions reach the trapped ion cell. An optional section can also be added that contains a collision cell for reacting or annealing the ion population before it reaches the trapped ion cell. These latter two sections have not been used for the results described here. Currently, the source is floated at a potential of +5 to +50 V and positive ions are extracted by a −100 to −950-V field. Typically, the field free voltage equals the extraction voltage. As expected, higher extraction/field free voltages increase ion transmission through the ion guide. Following extraction and focusing, the ion beam undergoes a 10° bend before exiting the vacuum chamber housing the source and source ion optics. This bend allows for separation of ionic and neutral particles; the neutral beam is dumped to the side of the orifice between the source chamber and the middle chamber (Fig. 2). Given the enormous quantity of material exiting the source, most of which is neutral, dumping the neutral beam at this early point in the ion guide greatly assists in keeping the remainder of the ion guide clean. It also prevents neutral particles from traveling along with the ionic particles and contaminating the trapped ion cell. The design and position of the einzel lenses optimize focusing through the orifices with minimum aberration, which enhances total ion throughput. The focusing characteristics of an einzel lens depend on the ion energy and may explain the mass dependence in the focusing characteristics of the lenses in our system. This is more pronounced for silicon clusters than for carbon clusters for a given mass range and undoubtedly reflects the kinetic energy distribution of the particles produced by the source.

The axis of the majority of the ion guide is positioned along the axis of the magnetic field of the superconducting magnet used for the FTICRMS. As discussed above, the source, electron gun, and first few elements of the ion guide are rotated 10° off of this axis. This magnet (see below) has significant fringing fields along the bore axis. Despite the obvious disadvantages of such fringing fields, they do have the significant advantage of assisting ion transmission through the electrostatic ion guide and into the trapped ion cell. We observe a pronounced increase in the ion current reaching the trapped ion cell as we increase the strength of the magnetic field. For example, at a constant field free voltage of −300 V, an increase of the magnetic field by a factor of 1.4 from 3.7 to 5.3 tesla increases the time averaged ion current at the trapped ion cell from 140 to 200 pA at laser rep rate of 50 Hz. Further enhancement of the ion throughput can be realized by increasing the ion guide voltage. For example, at constant magnetic field of 5.3 tesla, an increase of the extraction/field free voltage from −300 to −500 V increases the time averaged current at the trapped ion cell from 200 to 400 pA. This increase in ion current results totally from an increase in the throughput of *higher mass particles*. Fig. 3 illustrates the mass-dependent transmission efficiency as a function of ion guide field free voltage. This demonstrates how lower extraction/field free voltages discriminate against the larger mass particles.

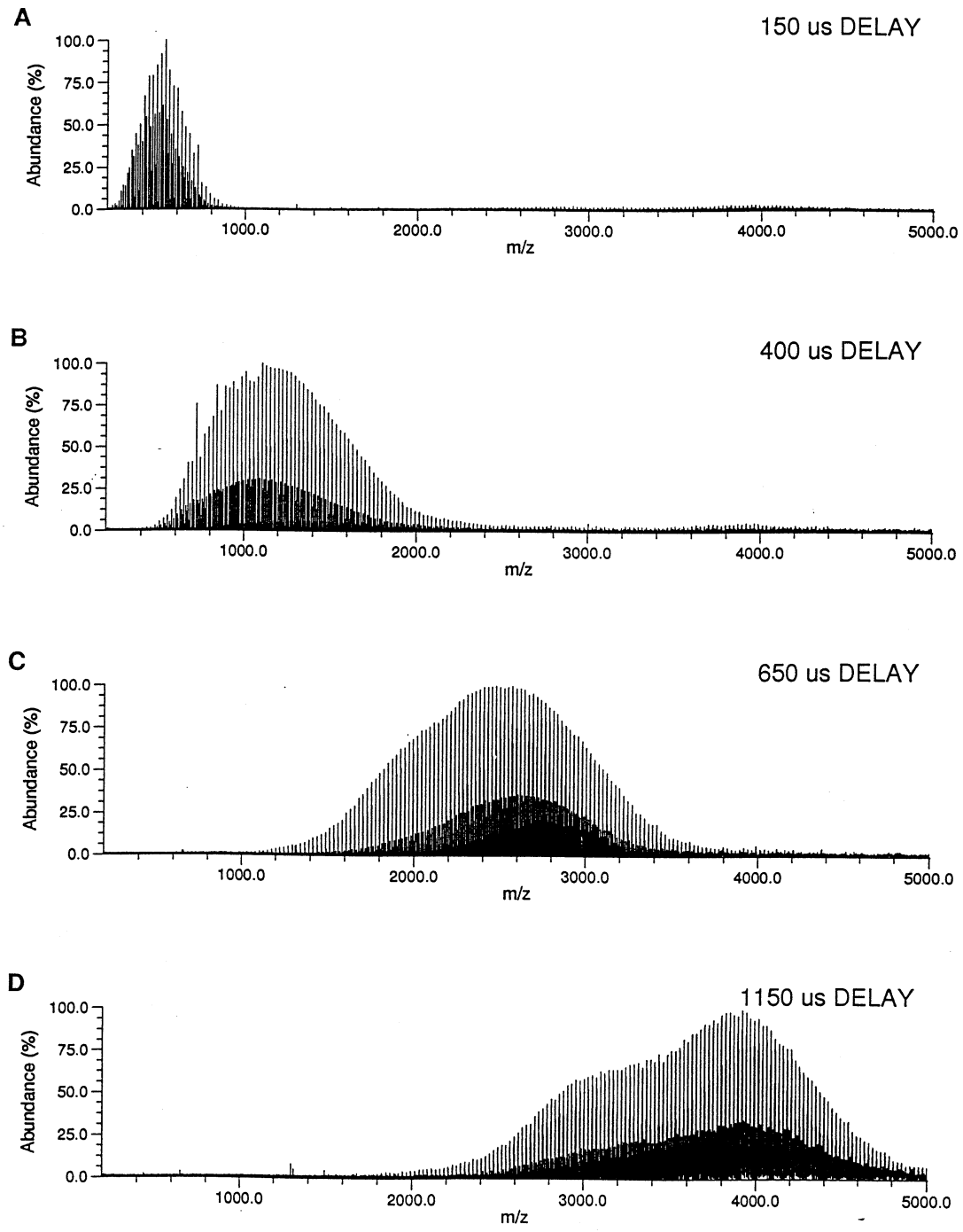

Fig. 5. Variation of C_n^+ population contained in the trapped ion cell as a function of time required to arrive in the ion cell after the ablation laser is fired. There is a smooth variation in arrival time in part due to the velocity distribution and the long flight path of 2 m. The arrival time distribution also varies with mass; this may be caused by a mass dependence in the ion energy distribution, a mass dependence in the ion residence times in the source, or a combination of both. The arrival time distributions can be exploited to restrict the mass distribution and ion loading in the trapped ion cell.

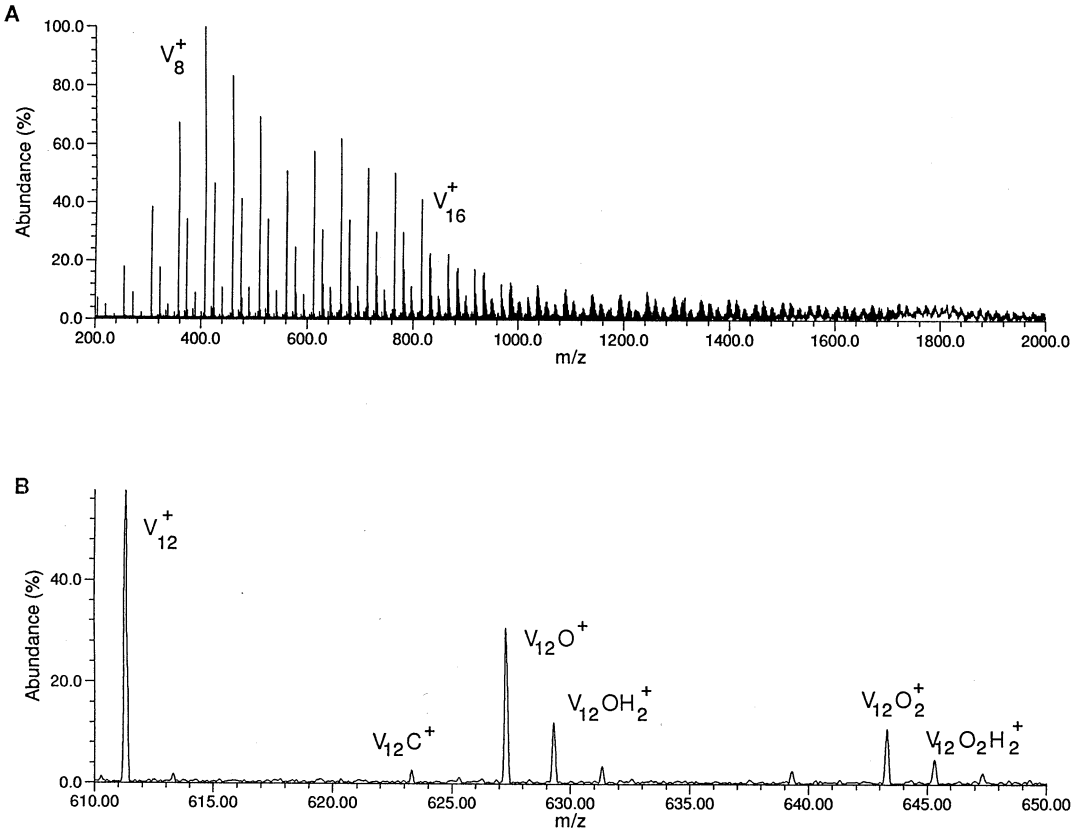

Fig. 6. (A) Distribution of vanadium cluster positive ions extending out to V_{33}^+. (B) Mass scale expansion showing the clusters present containing 12 vanadium atoms. Impurity atoms include carbon, oxygen, and hydrogen.

2.3. Loading the trapped ion cell: ion kinetic energy

Following their traverse through the electrostatic ion guide, the ions are transferred to the trapped ion cell located in the large homogeneous region of the split pair magnet. Here they can be held for milliseconds to hours for detection and characterization FTICRMS techniques. Just prior to reaching this cell, the ions are retarded by an exponential ion deceleration lens [8] to near thermal velocities. The next-to-last element of the deceleration lens stack is used as a focusing element to maximize transmission of the ion beam through the pumping aperture located on the ion guide side of the trapped ion cell. As discussed above, particles arrive in a 300–1000-μs-wide pulse that is selectively gated into the trapped ion cell. The gating sequence is synchronized with the output of the ablation laser and starts with lowering the potential of the ion cell trapping plate nearest the ion guide. This potential is kept low (-9 V) for a selected time interval to admit all or part of the positive ion burst into the trapped ion cell. The trapping plate is then returned to its full potential (3–9 V) to retain the ions in the ion trap. A 300-μs pulse of nitrogen or argon is introduced to assist in ion capture by collisionally removing excess kinetic energy and collapsing the ion cloud to the center of the cell. (Note that radial ion loss is greatly reduced in this instrument. Ions have been held in the trapped ion cell for >10 s at 10^{-3} Torr without a reduction in the ion population.)

The source/ion guide arrangement described above is capable of producing very narrow ion kinetic energy distributions. The optimum bias potential for

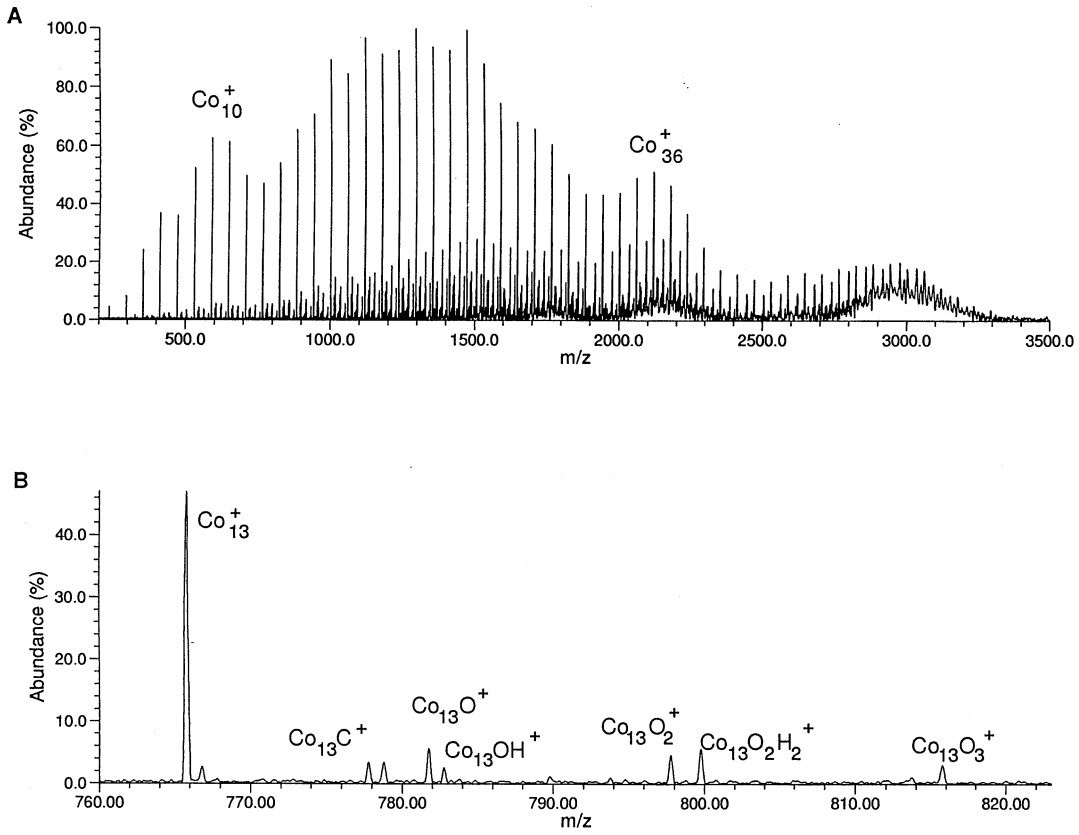

Fig. 7. (A) Distribution of cobalt cluster ions extending out to Co_{56}^+. (B) Mass scale expansion showing clusters containing 13 cobalt atoms. In addition to the dominant bare metal clusters, a significant fraction of clusters are present with up to three oxygen atoms and up to two hydrogen atoms.

the cluster source lies at +5 to +7 V for carbon clusters. These ions are efficiently stopped and held with a back trapping plate potential of +3 to +9 V. The front trapping plate potential is "gated open" by dropping its voltage to −9 V for the 0.3-ms loading time. Few ions are trapped with a source potential outside this range; less negative front trapping plate potentials result in ions with insufficient kinetic energy to enter the trapped ion cell whereas more negative potentials result in ions with sufficient kinetic energy to pass through the +3-V stopping potential on the trapping plate. The apparent discrepancy where +3 V on the trapping plate can stop ions generated at 5–7 V indicates that the nominal source potential itself is not necessarily representative of the potential of the ions leaving the source region. Based on our various experiences in operating the source, the ion potentials and energy distributions depend in a complex way on the source conditions, the cluster material, and the characteristics of the initial acceleration of the ions out of the source. We have also observed that metal clusters require a significantly higher source voltage (20–60 V) for the clusters to reach the trapped ion cell as compared with carbon clusters. An exception to this is the metal atomic ion, which is readily transmitted through the ion guide and trapped in the ion cell even at low (5–7 V) ion source voltage. Whether the need for a higher source voltage for metal clusters is due to thermochemistry of cluster growth, the details of cluster ion formation, or greater slippage in the helium flow relative to carbon clusters is unknown.

2.4. Fourier transform ion cyclotron resonance mass spectrometer

The total ion population in the trapped ion cell is detected by coherent excitation of their cyclotron motions followed by digitization of the current induced in two parallel plates positioned perpendicular to the ion motion. This time domain signal is Fourier transformed into the frequency domain; the frequency spectrum is then calibrated in terms of ion mass. Typical detection conditions are: excitation: (a) low mass by using rf chirp rate of 4000 Hz/μs; frequency range, 0.5 to 8000 kHz; rf intensity, 120 V_{p-p}; (b) higher mass by using SWIFT (Finnigan FTMS, Madison, WI) [9] excite with 1–2-Mbyte transform; frequency range, 0.8–800 kHz; rf intensity, 75 V_{p-p}. Additional conditions are: 12-bit digitization rate: 8 MHz (low mass detection) or 1.6 MHz (high mass detection) or 400 kHz (heterodyne detection); transient length, 1–60 s. The cylindrical trapped ion cell used in these experiments is 11.4 cm i.d. $\times$ 8.9 cm long. The ion excitation and signal collection and processing is done with a Finnigan FTMS Odyssey (Finnigan FTMS, Madison, WI) data station.

The trapped ion cell is designed to hold a large quantity of ions for improved sensitivity. The availability of a large homogeneous volume for the magnetic field allows use of very large cell volumes with improved sensitivity. Several cell geometries have been tested: 2.5 cm $\times$ 2.5 cm $\times$ 7.5 cm rectangular, 2.5 cm $\times$ 2.5 cm $\times$ 15 cm rectangular, and 11.4 cm i.d. $\times$ 8.9-cm long cylindrical cell. The elongated rectangular cells produce large signal-to-noise for electron ionization of admitted gases. For example, electron ionization of perfluorotributylamine present at 5×10^{-8} Torr produces sufficient number of ions to readily saturate the preamp electronics. Reducing the electron emission current to avoid saturation, the observed mass spectrum uses the full dynamic range of the 12 bit ADC converter on a single scan. If the most abundant ions are removed by careful on-resonance ejection, the signal observed for the ^{13}C isotope of CF_3^+ at mass 70 (previously present at 1% of the most abundant ion) still has a signal-to-noise of 100 with a single scan. Thus, the effective dynamic range of the trapped ion cell is limited to 10,000:1 by the premature saturation of the present preamp, and the dynamic range of the ion signal from a single scan is limited to 4000:1 by the 12-bit ADC. Such a large dynamic range confirms these trapped ion cells' capability to hold the large quantity of ions that is needed for high sensitivity detection over a wide range of ion masses. The studies discussed below use the 11.4-cm-i.d. $\times$ 8.9-cm-long cylindrical trapped ion cell because only the cylindrical cell produces high sensitivity with minimal loss of mass resolution. The success of our system to both generate and detect such a wide range of sizes is readily shown in Figs. 4(b) and 5(d) for silicon and carbon clusters, respectively.

The superconducting magnet portion of the FTICRMS was custom built to our specifications by Oxford Instruments. It is a split-pair design that allows access to the magnet's homogeneous region through four tubes, 4.8 cm in diameter, placed 90° apart perpendicular to the magnet's solenoid bore. The cryostat contains two superconducting magnets on either side of these tubes. The main bore along the magnetic field axis is a 316SS tube, inner diameter of 20 cm, with knife-edge sealing flanges on all ports. The homogeneous region is a cylinder 2.5 cm in diameter and 12.5 cm long with a superconductor-shimmed homogeneity of 8 parts in 10^5. A by product of the field strength of 5.3 tesla with the split-pair design and the large bore is a significant fringe field along the bore axis. While this fringing field requires careful selection of magnetic-field compatible components in the instrument and surrounding environment, as described above, it also aids in guiding the ions through the electrostatic ion guide and into the trapped ion cell.

The vacuum chamber is designed for high gas conductance and pumping speed. With the homogeneous region offset from the cryostat center and only 38 cm from the cryostat's end, a conductance of $\sim$3000 L/s is achieved at the cell. This is matched by the pumping station's cryopump (1000 L/s; 4000 L/s for water) and liquid nitrogen trapped diffusion pump (2500 L/s). This configuration allows high pressure gas pulses, admitted through one of the 4.8-cm tubes and directed at the trapped ion cell, to be used for

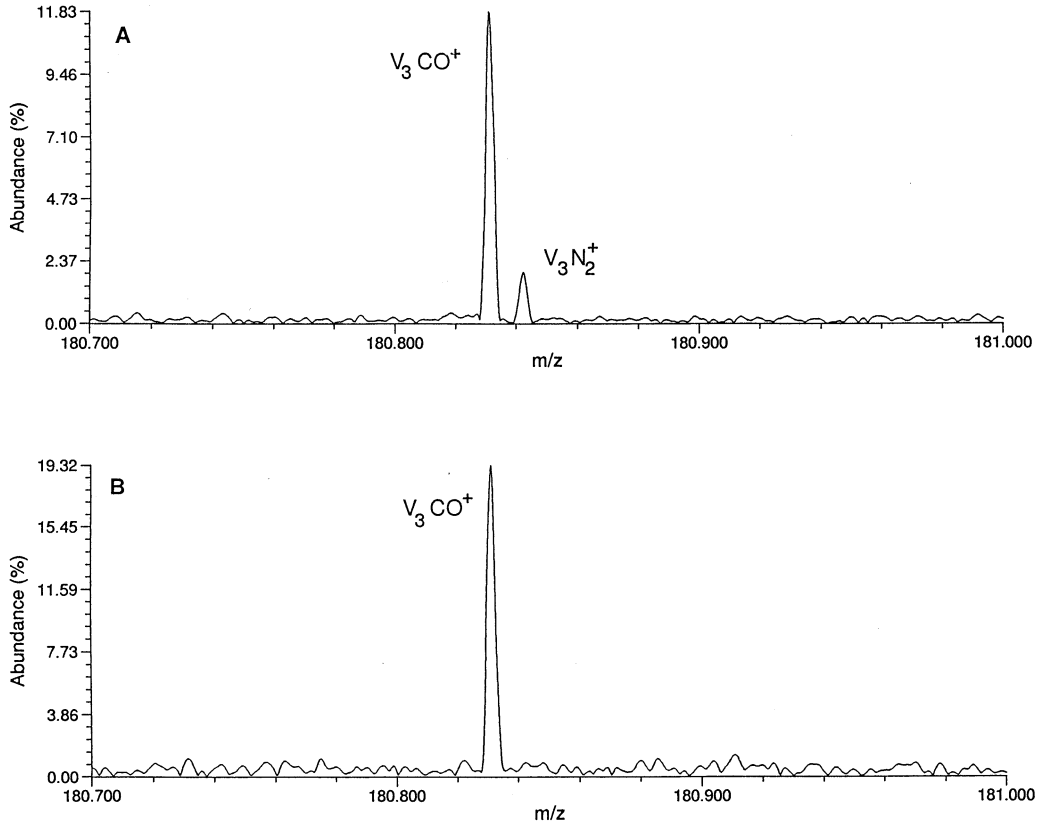

Fig. 8. Comparison of V_n^+ mass spectra near m/z 181 for $V_3CO^+/V_3N_2^+$ doublet taken with (A) nitrogen as stabilization gas or (B) argon as stabilization gas. In several instances, reaction with nitrogen is observed to produce mono- and di-nitrogen containing ions as shown in (A). Use of argon eliminates production of any nitrogen containing ions, demonstrating that they are produced in reactions of vanadium clusters with the high pressure N_2 pulse in the trapped ion cell. Argon is not observed to undergo association reactions with the ions.

collisional relaxation as well as reaction with the trapped ion population. A 0.3 ms, 0.01-Torr gas pulse of argon can be pumped away, achieving a pressure of $\sim 1 \times 10^{-8}$ Torr in ~ 2 s. Such a gas pulse is used to relax trapped ions to the center of the cell, e.g. in quadrupolar excitation, without the additional use of the rf quadrupolar excitation field.

3. Results and discussion

This home-built FTICRMS with its custom split-pair magnet coupled to the external ion source is a versatile instrument. The external source is capable of producing charged particles at least as large as 1–2 nm from a multitude of elements or molecules. The FTICRMS can be used in conjunction with the external source or as a stand-alone, high performance instrument. Application of this system as a combined instrument for the detection and characterization of large particles of various materials is discussed below.

3.1. Carbon and silicon clusters

We have synthesized particles of carbon and silicon by using targets of the respective elements. The resulting particle size distributions are shown in Figs. 4 and 5, respectively. The size distribution is depen-

dent upon "aging" the target rod. Initial particle sizes obtained from a fresh silicon rod, shown in Fig. 4(a), are smaller than the particle sizes obtained after repeated ablation of material from the rod, Fig. 4(b). Changes in the particle size distribution seem to occur in abrupt jumps rather than evolving slowly, probably due to a transition through an SiO_2/Si interface. The reasons behind these changes are unclear. For silicon, it appears to be related in part to the removal of a persistent oxide from the surface. Large silicon particles do not appear as long as the size distribution contains a large fraction of partially oxidized particles. This explanation does not hold for carbon that does not form a detrimental surface oxide. Possibly the formation of large particles is enhanced as the laser cuts channels into the rod [10]. These channels may serve to temporarily confine the ablated species over the rod, forming high pressure zones that assist particle growth. The appearance of large particles may also be correlated with the formation of a thick coating of ablated material over the interior of the source channel and, possibly, the partial blockage of the source nozzle aperature with small particles.

The carbon particle distribution in Figs. 5(a)–5(d) extends out to greater than 400 carbon atoms with the larger clusters being more intense than the smaller clusters. This is the first time that such an extended and intense large carbon cluster distribution has been seen from a pure carbon aggregation source [11]. Large carbonaceous particles have been in the mass spectrum of flash evaporated benzene soot that consists of various polymerized polyaromatic hydrocarbons [12] and in the laser ablation of polyphenylene sulfide [13]. Observed cluster size has been successfully modeled as a kinetic-limited growth based on the concentration of ablated particles [13]. This model does not account for the observed odd/even alteration in intensities nor for the disappearance of the odd-numbered clusters when thermalized [14].

The synthesized carbon particles shown in Fig. 5(d) (150–400 atoms) contain far more atoms than the synthesized silicon particles shown in Fig. 4(b) (4–40 atoms). A number of factors contribute to the growth kinetics that lead to the observed particle distributions. These factors include cluster binding energies that affect growth rates, feedstock ion and neutral densities, diffusive losses, and residence times in the source. However, another significant factor involves the sizes of the initial feedstock species ablated from the target surface. Laser evaporation of silicon produces both atomic and molecular ions and neutrals. In the ion fraction, Si^+ is the primary species but molecular ions containing up to at least six atoms are also produced [15]. The evaporated silicon neutral species follow a distribution similar to the ionic species [16]. In contrast, laser evaporation of carbon produces mostly molecular species. The positive ion distribution consists of 3–27 atom clusters with C_{11}^+ and C_{15}^+ being the most abundant [17]. The neutral distribution consists of 1–6 atoms with an abundance maximum at C_3 [18]. Under certain conditions, the size distribution increases markedly without the use of an aggregation gas, producing cluster ions as large as C_{120}^+ with a maximum at 60–70 atoms [9]. (Note that larger clusters and shot-to-shot reproducibility in size distribution require a gas aggregation source such as the one used in our instrument.) This marked increase in the size of ionic carbon clusters presumably coincides with a marked increase in the size of neutral carbon clusters. With the average starting size for carbon cluster ions 12–60 times greater in atom number than silicon and for the neutral molecules 3 times greater than for silicon, then, all else being equal, gas aggregation of these species should produce larger particles for carbon than for silicon. (The neutral molecules will presumably have grown as well, but their size distribution cannot be determined.) The observed particle sizes for carbon ions is, on average, ten times greater than for silicon in terms of atom number and four times greater in terms of mass. The size of the initially evaporated species appears important in determining the relative particle sizes in these two systems.

3.2. Cobalt and vanadium clusters

A distribution of ions is generated from a vanadium or a cobalt rod that include the pure element as well as mono- and di-oxides or hydroxides of the element as shown in Figs. 6 and 7, respectively. The

high mass cutoff in the size distribution is believed to result from low association probabilities coupled with the limited residence time in the source. High mass transmission by the ion guide is not a limitation because it readily transmits ions of higher mass (vide infra). Lengthening the residence time is expected to extend the size distribution.

Pulsing nitrogen into the vacuum chamber removes excess kinetic energy from the ions, allowing for their efficient capture in the trapped ion cell. However, in the case of vanadium, reaction with the nitrogen quenching gas is observed. Fig. 8 illustrates this with a comparison between use of nitrogen as the cooling gas [Fig. 8(a)] and argon as the cooling gas [Fig. 8(b)]. This high resolution mass spectrum clearly separates V_3CO^+ (which is generated from C/O impurities in the source) from $V_3N_2^+$. Mass accuracies of 0.1 to 2 ppm are obtained with a one-point mass calibration (at $V_3C_2^+$) as shown in Table 1. There is no sacrifice in mass accuracy due to the limited magnetic field homogeneity of 8 in 10^5. Note the variety of compositions present as well as both mono- and di-nitrogen containing ions. These nitrogen-containing ions disappear when argon replaces nitrogen as the cooling gas. Subsequent studies use argon to avoid undesired reactions. No association reactions with argon have been observed.

Table 1
Mass measurement accuracy for V_n^+ [a]

Ion ID	Calculated mass	Δm (ppm)
V_3^+	152.83145	−0.72
V_3H^+	153.83929	−0.01
V_3C^+	164.83145	−0.42
V_3CH^+	165.83928	−0.15
V_3N^+	166.83452	−0.36
$V_3CH_2^+$	166.84765	+0.18
V_3O^+	168.82636	−0.36
V_3OH^+	169.83419	−0.06
$V_3C_2^+$	176.83145	0.00
$V_3C_2H^+$	177.83928	−0.39
V_3CN^+	178.83452	+0.34
$V_3C_2H_2^+$	178.84710	+0.06
V_3CO^+	180.82636	+0.28
$V_3N_2^+$	180.83759	−0.39
V_3COH^+	181.83419	0.00
V_3NO^+	182.82943	−0.16
$V_3O_2^+$	184.82127	+0.22
$V_3O_2H_2^+$	186.83692	−0.86
$V_3C_3^+$	188.83145	+0.53
V_4N^+	217.77852	+1.1
$V_4N_2^+$	231.78159	−2.1

[a]Mass measurements based upon one point mass calibration for $V_3C_2^+$ with confirmation of number of vanadium atoms present by observed vanadium isotopic distributions. Accuracy of mass measurement is confirmed for V_3^+ and $V_3N_2^+$ (which is present only when N_2 is pulsed into the system).

3.3. Demonstration of FTICRMS instrument performance by using synthesized clusters

In situations where very high sensitivity is required, it is desirable to examine a large ion population in the cell. Unfortunately, such a large ion population usually results in loss of other desired performance characteristics. This FTICRMS instrument is designed to contain a large ion population in the trapped ion cell although maintaining correct isotopic distributions. This is demonstrated in Fig. 9(a), which shows the high mass distribution for carbon clusters.

The distribution is dense but individual isotopic groupings cannot be discerned due to the wide mass range displayed. Mass scale expansions in Figs. 9(b)–9(d) reveal the detailed isotopic distribution with an inherent mass resolution of 10,000 at m/z 4,000. Table 2 lists the calculated and measured isotope distributions for the C_{332} cluster. This agreement is typical across the observed mass range. Such high mass resolution with a mass range this broad requires the large cell used here (11.4 cm i.d. × 8.9-cm-long cylindrical cell). In addition, the ion excitation requires the well-defined SWIFT process available with the data system used. Using an rf chirp excitation produces a poorly defined mass spectrum as shown in Fig. 10.

Higher mass resolutions can be obtained by narrowing the size distribution prior to loading the ion cell. This allows us to maximize the numbers of the ions of interest to the extent that a very high signal-to-noise mass spectrum can be obtained in a single scan. In the present configuration of our instrument, we use the mass-dependent arrival times to select a

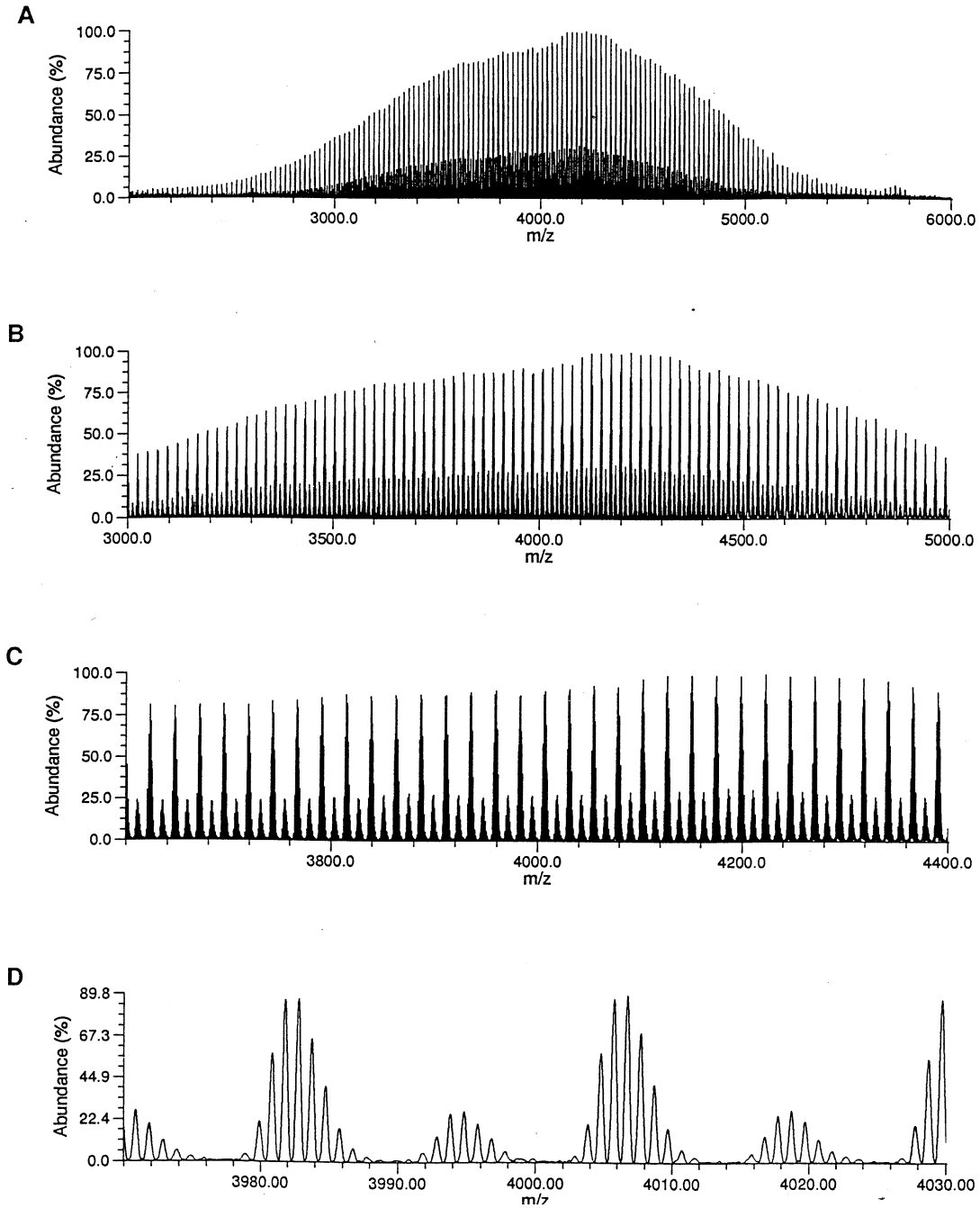

Fig. 9. Distribution of high mass C_n^+ in the 11.4-cm-i.d. × 8.9-cm-long cylindrical trapped ion cell. This spectrum is the sum of 250 scans. (A) Full mass distribution with an ion transient length of 2.3 s. Note the darker region at roughly 1/3 of the full ion intensity, which is due to the odd-numbered carbon clusters, C_{2n+1}^+. (B) Same spectrum as in (A) with a mass scale expansion in the range of 3000–5000 U. The odd/even alternation in intensities is more clearly discernable. (C) Same spectrum as in (A) with a mass scale expansion in the range of 3600–4400 U. The carbon isotopic envelope appears but separation of the individual isotopes is not discernable due to limited printer resolution. (D) Same mass spectrum as in (A) with mass scale expansion in the range of 3950–4050 U. The individual carbon isotopes are base-line separated with a resolution of 10,000 at mass 4000. The simultaneous acquisition of high resolution with very large mass distribution present in the cell required the large volume cell used here as well as the well-defined SWIFT excitation electronics.

Table 2
Calculated and measured isotope distribution for C_{332}^+

Elemental composition	Nominal mass	Calculated relative abundance (%)	Measured relative abundance (%)	Deviation
$^{12}C_{332}$	3984	12	7	−5
$^{12}C_{331}{}^{13}C$	3985	44	33	−11
$^{12}C_{330}{}^{13}C_2$	3986	81	75	−6
$^{12}C_{329}{}^{13}C_3$	3987	100	100	−
$^{12}C_{328}{}^{13}C_4$	3988	91	96	+5
$^{12}C_{327}{}^{13}C_5$	3989	67	71	+4
$^{12}C_{326}{}^{13}C_6$	3990	40	43	+3
$^{12}C_{325}{}^{13}C_7$	3991	21	21	0
$^{12}C_{324}{}^{13}C_8$	3992	9	9	0
$^{12}C_{323}{}^{13}C_9$	3993	4	4	0

portion of the ion packet mass distribution to be loaded into the trapped ion cell. Use of a carbon rod readily produces a broad size distribution with mass-dependent arrival times to the trapped ion cell. Fig. 5 demonstrates how we can use the time dependence for the arrival of carbon clusters to the cell to generate a

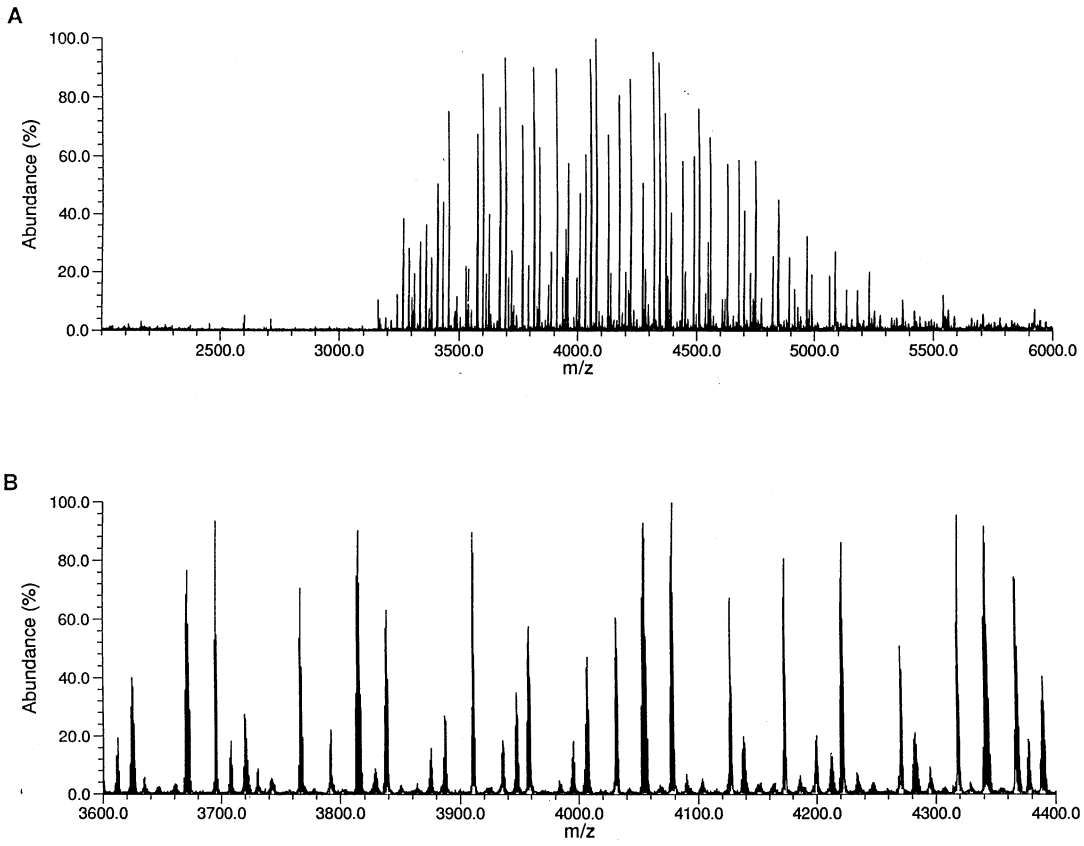

Fig. 10. Mass spectrum taken under the same conditions as Fig. 9(A) with the exception that a standard rf chirp is used. Under no chirp conditions could a complete mass spectrum be obtained. We believe this is due to the dense ion loading present in the trapped ion cell.

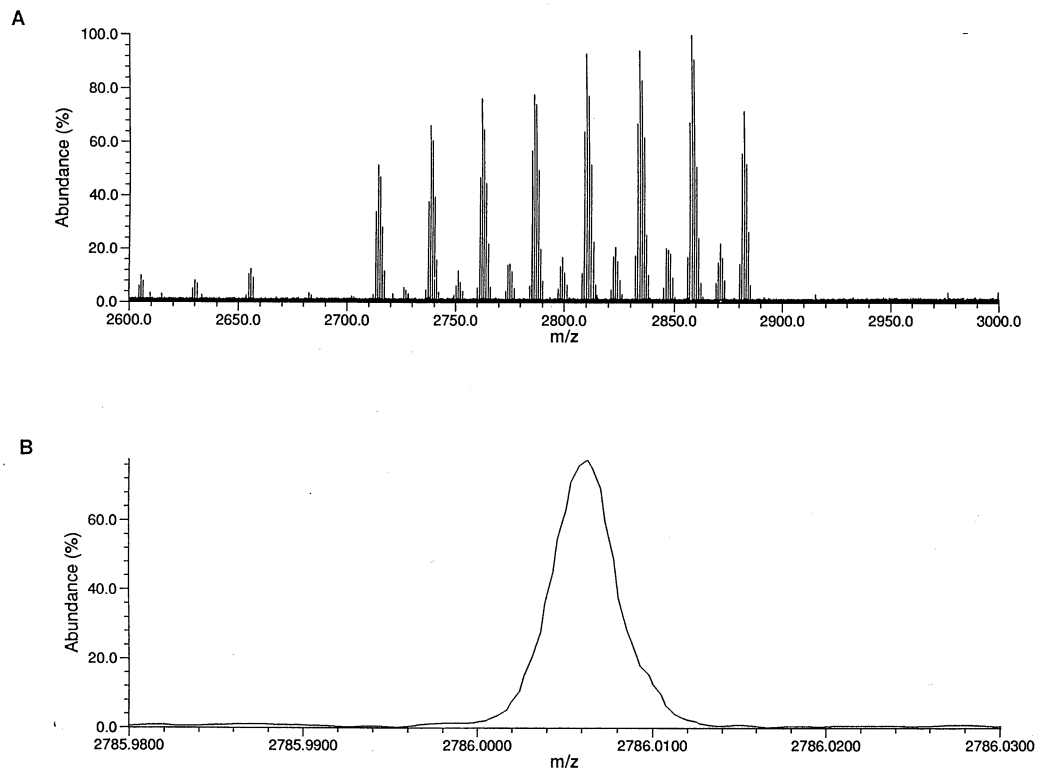

Fig. 11. Ultrahigh mass resolution of C_n^+ in the mass range of 2700–2900 U. Ions outside this mass range were ejected by using standard SWIFT techniques. This is a single scan mass spectrum with an ion transient length of 60 s obtained at a base pressure of 1×10^{-9} Torr. Note that a 0.01-Torr nitrogen gas pulse is used to efficiently trap ions in the cell and a second 0.01-Torr nitrogen gas pulse is used after ion ejection to refocus ions to the center of the cell. (A) Complete mass spectrum of the clusters present after ejection. (B) Mass scale expansion at $^{12}C_{230}{}^{13}C_2^+$ demonstrating mass resolution of 640,000.

series of mass spectra that center on different mass range. These spectra are collected by using different "gate open" times for introducing the ion packet into the trapped ion cell. Additional tuning of the ion guide can further narrow the size distribution by one-third without loss of ion intensity for the trapped ion population.

The ultrahigh mass resolution capabilities of our FTICRMS instrument are beautifully illustrated in the cluster mass spectra. Note that we obtain ultrahigh mass resolution despite the limited magnetic field homogeneity (8 parts in 10^5). At high ion loadings, a mass resolution of 10,000 at m/z 4000 is attained which equals the measured field homogeneity for this magnet. Much higher resolution (12,000,000) at low mass (H_3O^+) and low ion loadings has been attained. Greatly increased resolution is attainable at high mass as well by reducing the extremely large ion population. Limiting the mass range to m/z 2700–2900, a resolution (FWHM) of 640,000 is achieved as shown in Fig. 11. There are two points to note here. First, this is a single scan with improved signal-to-noise compared with the complete mass spectrum. Second, this resolution exceeds not only the magnetic field homogeneity of 12,500, but also the background pressure-limiting resolution of 140,000. The ion transient does not decay as rapidly for larger masses because collisional loss of the excited ion packets' coherence of motion is reduced [1a]. Collision of a massive ion with a light molecule, in our case water, only slightly alters the ion's velocity. Multiple collisions are now required for significant effect. The more

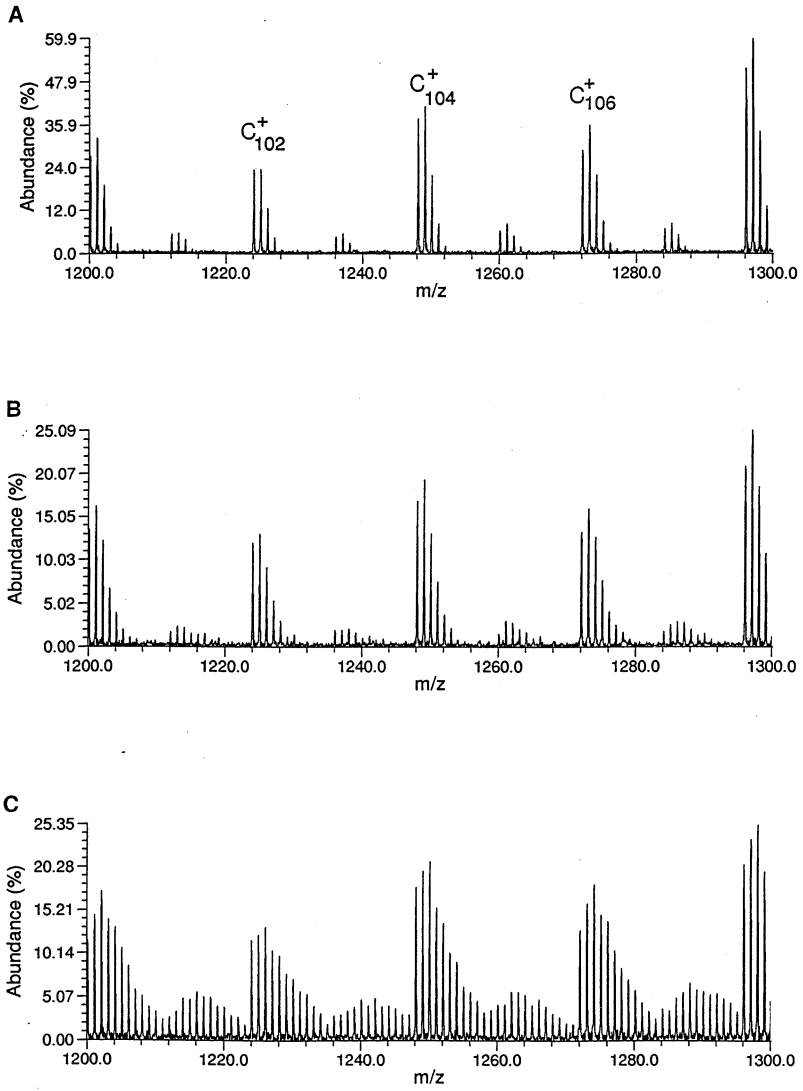

Fig. 12. Sequence of spectra showing reaction of C^+_{100} to C^+_{108} with nitrogen in the source. Pressure of gas in source maintained at 9 Torr. (A) No nitrogen present. (B) Nitrogen present at 2 Torr with the balance helium. Note the "apparent" distortion in carbon isotopic distribution due to incorporation of 1–3 nitrogen atoms/cluster. (C) Conditions as in (B) with additional use of an electron gun to create a continuous plasma in the source. Nitrogen incorporation has significantly increased as compared to the spectrum in (B) taken with no electron gun.

massive the ion, the longer the transient length. Thus, for heavier ions, high homogeneity magnetic field and ultrahigh vacuum are not as important to achieve high mass resolution. This has thus far been observed for all of the larger carbon clusters; none of the other systems produced sufficiently large ions thus far.

The enhanced performance of our FTICRMS instrument in combined high mass resolution and accurate mass measurement is demonstrated in the reaction of nitrogen with carbon particles. Nitrogen is introduced into the source with the helium cooling gas to react with the growing ionic carbon particles. Addition of nitrogen (~20% in helium) alters the apparent isotopic distribution as shown in Figs. 12(a) and 12(b). The distortion is most noticeable for the

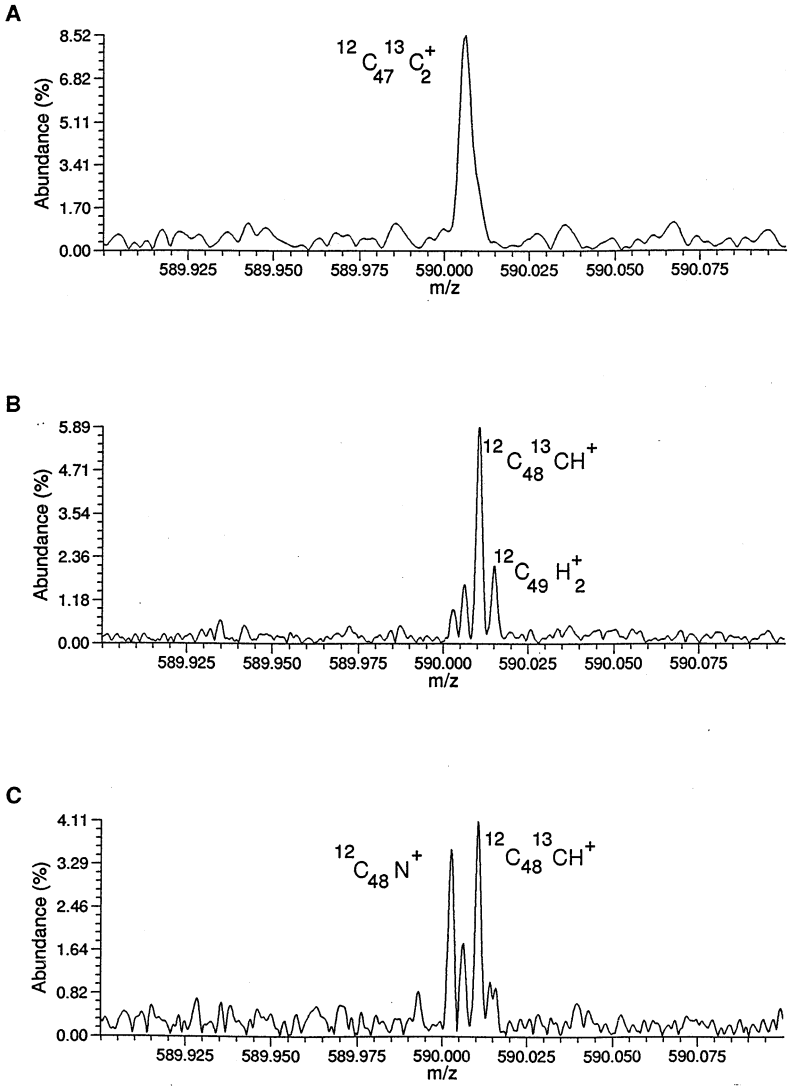

Fig. 13. High resolution mass spectra near *m/z* 590 for carbon clusters under conditions as in Fig. 12 illustrating addition of both hydrogen and nitrogen to the carbon clusters. A mass resolving power of >110,000 required for separation of individual peaks. (A) Pure helium in source at 9 Torr. The dominant peak contains only carbon with a weaker, unresolved satellite peak at higher mass that contains hydrogen. Mass resolving power of 140,000 is insufficient because the two ions are of unequal abundance. (B) Helium with 2 Torr nitrogen in source. Higher mass resolution (300,000) than in (A) now resolving nitrogen- and hydrogen-containing ions from pure carbon ion. Note the dominance of hydrogen-containing peaks. (C) Helium with 2-Torr nitrogen in source as in (B) with additional use of source electron gun to enhance reaction. The nitrogen peak is now comparable in intensity to that of $^{12}C_{48}{}^{13}CH^+$ illustrating the enhanced reaction provided by use of the electron gun. Mass resolving power comparable to (B).

weaker odd-numbered particles, C_{2n+1}^+. Increased nitrogen concentration diminishes the ion signal to zero without increasing nitrogen content in the clusters. However, use of the electron gun to create a continuous plasma in the source increases both the ion signal and extent of nitrogen incorporation as shown in Fig. 12(c). The extent of nitrogen incorporation can be inferred by comparing the relative intensities of the masses in each cluster "envelope" with that expected from isotopes of carbon-12 and carbon-13 alone.

However, with increasing nitrogen content per cluster, it becomes increasingly difficult to discern the relative contribution of the various species to each peak. This is where the ultrahigh mass resolution capabilities are particularly useful. Fig. 13 shows a mass spectrum taken near m/z 600 under increased mass resolution. Multiple ion populations are revealed within the mass envelope of a given cluster. Not only is nitrogen present, but hydrogen as well. Mass measurement accuracies of better than 1 ppm verify the composition assignments.

4. Conclusions

The high performance capabilities of the combined source, ion guide, and trapped ion cell are demonstrated in this unique instrument. The intense external source allows synthesis of a wide variety of species. Its pulsed nature is well adapted to the pulsed operation of an FTICRMS. High ion transmission efficiency coupled with a large trapped ion cell loading capacity allows detection of broad mass ranges simultaneous with high mass resolution, accurate mass measurement, and reliable isotopic abundances. High gas pressure operation (0.01 Torr) at the trapped ion cell of the FTICRMS does not compromise low pressure, high mass resolution detection due to the high conductance, rapid pump-down design of the vacuum system. The limited magnetic field homogeneity of 8 parts in 10^5 does not compromise performance either. Mass resolution of 640,000 at m/z 2800 exceeds the expected pressure-limited resolution of 140,000. Mass resolution of 12,000,000 at m/z 19 is readily attained as well.

References

[1] (a) B.E. Winger, S.A. Hofstadler, J.E. Bruce, H.R. Udseth, R.D. Smith, J. Am. Soc. Mass Spectrom. 4 (1993) 566; (b) R.T. McIver Jr., Yunzhi Li, R.L. Hunter, Proc. Natl. Acad. Sci. USA 91 (1994) 4801; (c) Yunzhi Li, R.T. McIver, Jr., R.L. Hunter, Anal. Chem. 66 (1994) 2077.
[2] T.D. Wood, C.W. Ross III, A.G. Marshall, J. Am. Soc. Mass Spectrom. 5 (1994) 900.
[3] N.L. Kelleher, M.W. Senko, D.P. Little, P.B. O'Connor, F.W. McLafferty, J. Am. Soc. Mass Spectrom. 6 (1995) 220.
[4] G.T. Uechi, R.C. Dunbar, J. Am. Soc. Mass Spectrom. 3 (1992) 734.
[5] M.L. Mandich, W.D. Reents, V.E. Bondybey, in E.R. Bernstein (Ed.), Atomic and Molecular Clusters, Elsevier, New York, 1990.
[6] (a) P. Kofel, T.B. McMahon, Int. J. Mass Spectrom. Ion Processes 98 (1990) 1; (b) J.M. Alford, P.E. Williams, D.J. Trevor, R.E. Smalley, ibid. 72 (1986) 33.
[7] Ion guide trajectories calculated by using SIMION, Version 3.0, developed by D.A. Dahl, J.E. Delmore, Idaho National Engineering Laboratory, Idaho Falls, ID.
[8] M.L. Vestal, C.R. Blakley, P.W. Ryan, J.H. Futrell, Rev. Sci. Instrum. 47 (1976) 15.
[9] A.G. Marshall, T.-C. Wang, T.L. Ricca, J. Am. Chem. Soc. 107 (1985) 7893.
[10] A. O'Keefe, M.M. Ross, A.P. Baronavski, Chem. Phys. Lett. 130 (1986) 17.
[11] S.W. McElvany, M.M. Ross, J. Am. Soc. Mass Spectrom. 3 (1992) 268.
[12] H.Y. So, C.L. Wilkins, J. Phys. Chem. 93 (1989) 1184.
[13] W.R. Creasy, J.T. Brenna, J. Chem. Phys. 92 (1990) 2269.
[14] G. von Helden, M.-T. Hsu, N. Gotts, M.T. Bowers, J. Phys. Chem. 97 (1993) 8182.
[15] W.D. Reents, V.E. Bondeybey, Chem. Phys. Lett. 125 (1986) 324.
[16] R.E. Honig, J. Chem. Phys. 22 (1954) 1610.
[17] R.D. Knight, R.A. Walch, S.C. Foster, T.A. Miller, S.L. Mullen, A.G. Marshall, Chem. Phys. Lett. 129 (1986) 331.
[18] W.A. Chupka, M.G. Inghram, J. Chem. Phys. 21 (1953) 1313; R.E. Honig, ibid., 22 (1954) 126; R.J. Thorn, G.H. Winslow, ibid., 26 (1957) 186; J. Drowart, R.P. Burns, G. DeMaria, M.G. Inghram, ibid. 31 (1959).